Journal of Materials Chemistry A

PAPER

View Article Online
View Journal | View Issue

Cite this: J. Mater. Chem. A, 2018, 6, 11929

Surface termination effects on the oxygen reduction reaction rate at fuel cell cathodes†

Yuri A. Mastrikov, [ac] Rotraut Merkle, [*b] Eugene A. Kotomin, [ab] Maija M. Kuklja [c] and Joachim Maier [b]

The results of first principles calculations of oxygen vacancy and oxygen adsorbate concentrations are analyzed and compared for the polar (La,Sr)O and MnO_2 (001) terminations of (La,Sr)MnO_3 fuel cell cathode materials. Both quantities strongly depend on the average Mn oxidation state (La/Sr ratio). In thin symmetrical slabs, the cation nonstoichiometry also plays an important role by modifying the average Mn oxidation state. The surface oxygen vacancy concentration for the (La,Sr)O termination is more than 5 orders of magnitude smaller when compared to the MnO_2 termination. The vacancy and adsorbed oxygen migration energies as well as the dissociation barriers of adsorbed molecular oxygen species are determined. The encounter of adsorbed atomic oxygen and surface oxygen vacancy is identified as the rate determining step of the oxygen incorporation reaction. Since the increase of atomic and molecular oxygen adsorbate concentration is limited by the typical saturation level in the range of 20% for charged adsorbates, the overall oxygen incorporation rate is predicted to be significantly smaller for the (La,Sr)O termination.

Received 4th March 2018
Accepted 17th May 2018

DOI: 10.1039/c8ta02058b

rsc.li/materials-a

1 Introduction

Solid oxide fuel cells (SOFCs) continue to attract great attention as a promising source of ecologically clean and efficient electricity generation. The key factor, largely determining the SOFC performance, is the oxygen reduction reaction (ORR) rate at the surface with further oxygen incorporation into the cathode.[1–4] $La_{1-x}Sr_xMnO_{3-\delta}$ (LSM) was one of the first ABO_3-type perovskites employed as a SOFC cathode material, which is still used in the form of porous composites with the respective electrolyte material, to increase the average ionic conductivity. In our previous investigation,[5] we studied in detail oxygen adsorption, dissociation and migration on the (001) MnO_2-terminated LM surface while LaO one is much less studied.

For undoped $LaMnO_{3-\delta}$ (LM), the MnO_2 (001) termination was calculated to be the most stable termination;[5] however, with increasing Sr doping the (La,Sr)O termination is predicted to become energetically more favorable.[6] Also, for a given average cation composition, it is frequently found that the surface exhibits a higher Sr content and/or an increased ratio of A-site to B-site cations either already introduced during film preparation by pulsed laser deposition[7] or upon annealing.[8–10] Segregation effects are also supported by theoretical calculations.[6] Similar trends of A-cations and, in particular, Sr surface segregation were also found for perovskite $La_{1-x}Sr_xCo_{1-y}Fe_yO_{3-\delta}$ (LSCF, see *e.g.* ref. 11–13) solid solutions, emphasizing the importance of better understanding of defect formation and oxygen reduction kinetics on the AO-type termination.

When comparing the different (001) terminations of LSM, the fact that these terminations represent polar surfaces has to be properly taken into account. The formation of polar terminations is rather frequent for oxides. The physics and chemistry of a broad class of oxide polar surfaces are summarized, for instance, in review articles.[14,15] The pure polar terminations of a macroscopic sample are electrostatically unstable and must reconstruct to avoid the "polar catastrophe" due to a huge dipole moment. This could be achieved in several ways. In this paper, we assume that the LSM (001) surface polarity is negated by surface rumpling and the electron density redistribution near the surface. There are also other options to compensate for surface dipole moments, such as surface oxygen vacancy formation,[16] structural changes through the formation of extended structural defects such as steps and trenches,[17] or structural reconstruction through a complete rearrangement of the terminating planes into an ordered pattern of AO and BO_2 stripes.[18] However, a comprehensive study of these options, which strongly depend on particular experimental conditions, extends far beyond the goals of this article.

In the present paper, we analyze the oxygen vacancy ($V_O^{\cdot\cdot}$) formation, oxygen (both atomic and molecular) adsorption and dissociation on LSM (001) (La,Sr)O- and (001) MnO_2-terminated

[a]Institute of Solid State Physics, University of Latvia, Riga, Latvia
[b]Max Planck Institute for Solid State Research, Stuttgart, Germany. E-mail: r.merkle@fkf.mpg.de
[c]Materials Science and Engineering Department, University of Maryland, College Park, Maryland, USA

† Electronic supplementary information (ESI) available. See DOI: 10.1039/c8ta02058b

surfaces (also comparing with previous results for (001) MnO_2 (ref. 5,19,20)). To some extent, the nominal polarity of $(LaO)^+$ and $(MnO_2)^-$ layers may be decreased by surface rumpling and also by the electron density redistribution near the surface (see the discussion in Section 3.1). Nevertheless, the remaining polarity strongly modifies the defect formation and adsorption energies, and thus strongly influences the oxygen exchange surface reaction kinetics. It might also act as a driving force for surface reconstruction at elevated temperatures. Despite the importance of this phenomenon – also for related (Ba,Sr,La)-(Fe,Co,Mn)O_3 perovskites – it has rarely been systematically investigated. Also, the commonly neglected effect of different Mn oxidation states in slabs with different cation stoichiometry has to be taken into account. Based on our results, a semi-quantitative comparison of the oxygen reduction kinetics on LSM (001) MnO_2 and on (La,Sr)O termination layers is given. The focus of the present investigation is on the relative differences between the (001) (La,Sr)O and (001) MnO_2 terminations, rather than on absolute reaction rates or absolute values of defect energetics.

2 Computational details

In this study, LSM refers to all possible (La,Sr)MnO_3 compositions; the abbreviation LM represents Sr-free lanthanum manganate bulk or slabs, while LS25M is used for systems in which 25% of La ions are substituted with Sr, and LS50M for 50% Sr doping, respectively. While a high Sr content, such as in LS50M, is rarely used for SOFC cathode materials, it is still within the solubility limit[21] and allows us to explore a larger range of Mn oxidation states. Calculations were performed using the DFT method,[22] as implemented in the computer code VASP5.4.[23] Core electrons are substituted with US PAW[24] potentials (Table A1 in the ESI†), and the GGA-PBE[25] exchange–correlation functional is employed. To make the results comparable to our previous calculations on the MnO_2 termination (ref. 5,26,27), we here used the GGA approach without the Hubbard $+U$ term. Despite the fact that this neglect could affect the absolute values of reactions including electron transfer,[28–30] it is expected not to skew the relative difference of such reaction energies for different slab terminations, which are the main goal of the present study. The difference of $V_O^{\cdot\cdot}$ concentrations for AO and BO_2 terminations is the most important contribution to the slower O exchange kinetics at the AO surface (Section 3.4), and since the charges of the oxide ions in the surface plane do not differ much between AO and BO_2 terminations (Table A2†), the respective surface $V_O^{\cdot\cdot}$ formation energies will be similarly affected by the $+U$ correction for both terminations. For early 3d transition metals such as Mn, the formation energies of different negatively charged oxygen adsorbates on the respective oxides change monotonically with U.[31,48] While the magnitude of the $+U$ correction might vary according to the different number of electrons transferred to different adsorbed species (Table A5†), this difference in the correction is not expected to override the pronounced E_{ads} differences as shown in Fig. 7.

Moreover, it was shown that for the experimental orthorhombic geometry, such an approach correctly reproduces the A-type anti-ferromagnetic (AAF) structure of LM experimentally observed at low temperatures[26,32] and the basic defect properties of many ABO_3 perovskites and their solid solutions.[3,5,33–37] The kinetic energy cut-off is set to 520 eV. Brillouin zone sampling is performed by the Monkhorst–Pack scheme[38] with 30 and 20 k-points $Å^{-1}$ for the bulk and the surface calculations, respectively.

Depending on the temperature and degree of (non)stoichiometry, three types of structural distortions have been observed in $La_{1-t}MnO_{3-\delta}$, one rhombohedral $R\bar{3}c$ and two orthorhombic $Pnma$.[39,40] These distortions could be a combination of the octahedral tilting, rotation and Jahn–Teller octahedral deformation.[41] Energetically, the difference between rhombohedral and orthorhombic phases in the LM bulk does not exceed 0.05 eV per ABO_3 formula unit. Experimentally, the orthorhombic phase of LM can easily be converted into the rhombohedral one by annealing in N_2 at 600 °C,[42] indicating that both structures are very close in energy, whereas the ideal cubic perovskite is considerably (by ~0.3 eV) less favorable. Therefore, it is essential to introduce a lattice distortion into the modeling. The spin-polarization of B cations also strongly affects the energy of the structure. Diamagnetic solutions are considerably (by ≈1 eV) less favorable than magnetic solutions whereas the energies of FM and all high-symmetry A-, C-, GAF states lie close together, within 0.1 eV per formula unit. The choice of the exact magnetic structure is not expected to significantly affect the results, as long as it is consistent for all calculations (at cathode operating temperatures, LSM anyway loses its magnetic order and becomes paramagnetic).

In our slab calculations, we employed the ferromagnetic state (Mn in a high spin state) with a rhombohedral structure, which is lowest in energy. In this structure, the oxygen octahedra rotate alternately in all three main directions, whereas in the orthorhombic structure along the direction normal to the basal plane all octahedra rotate in the same direction (Fig. 1a and b). For defect calculations in the bulk, an 8 ABO_3-unit pseudo-cubic $2 \times 2 \times 2$ supercell was used. High-symmetry structures were constructed in such a supercell for 0, 25 and 50% relative Sr concentrations, creating bcc and simple cubic Sr-sublattices, respectively. Two concentrations of oxygen vacancies ($\delta = 0.125$ and 0.25) were simulated by removing neutral oxygen atoms. This leads to an increased electron density of the nearest Mn ions (thus, decreasing their oxidation state). The electron density inside the oxygen vacancy is negligible (≤0.1 e), and the vacancy can thus be denoted as a doubly positively charged defect, $V_O^{\cdot\cdot}$, in the standard Kröger–Vink nomenclature. The oxygen vacancy formation energies are calculated according to $E_{V_O^{\cdot\cdot}} = E(A_xB_yO_{z-1}) + 0.5E(O_2, \text{gas}) - E(A_xB_yO_z)$ for stepwise removal of O atoms from the $A_xB_yO_z$ supercells.

In the (001) surface calculations, seven-layer 2D symmetric slabs were used (*i.e.* sequence AO–BO_2–AO–BO_2–AO–BO_2–AO or BO_2–AO–BO_2–AO–BO_2–AO–BO_2; total thickness about $3.5a_0$ which corresponds to ≈14 Å), separated along the z axis by a $5a_0$ vacuum gap. The surface cell is made of eight AO or BO_2 units ($2a_0\sqrt{2} \times 2a_0\sqrt{2}$, Fig. 1c). There are two, eight and four

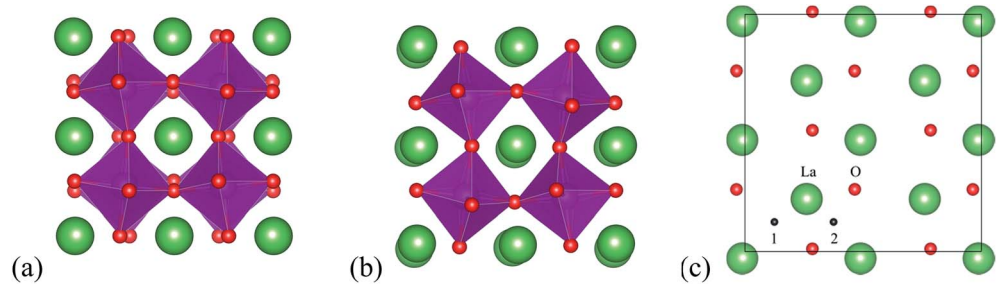

Fig. 1 (a) Oxygen octahedral rotation in all main directions in the rhombohedral structure, (b) along the normal to the basal plane direction in the orthorhombic structure, and (c) the (001) $2a_0\sqrt{2} \times 2a_0\sqrt{2}$ LaO-terminated surface cell of rhombohedral $LaMnO_3$ (LM). The two non-equivalent "hollow" adsorption sites are indicated by labels "1" and "2". Red and green symbols stand for O and La ions.

nonequivalent surface oxygen lattice sites for 0, 25 and 50% Sr concentrations, respectively. The removal/adsorption of a surface oxygen atom from these terminations (symmetrically on both sides) leads to a surface defect concentration of 12.5% (1/8 defect per AO or BO_2 surface formula unit). The lattice constants were optimised in the bulk defect calculations (leading to a small energy reduction, $\leq$0.05 eV per formula unit). For the slab calculations only the atomic coordinates were optimized, with the lattice constants kept fixed at the respective bulk values.

The calculated binding energy for a gas-phase O_2 molecule is -5.9 eV (the combination of pseudopotentials and exchange–correlation functionals used in the plane wave VASP code is known to overestimate the experimental value of 5.12 eV and thus the vacancy formation energy; however, this does not affect the differences of the defect and adsorbate formation energies that are the main focus of the present study. The calculated bond length of 1.23 Å is close to the experimental value of 1.21 Å). The lattice constants and angles in rhombohedral LM, LS25M and LS50M are $a_0 = 7.88$ Å, $\alpha = 90.85$; $a_0 = 7.81$ Å, $\alpha = 90.54$; and $a_0 = 7.77$ Å, $\alpha = 90.50$, respectively.

The oxygen adsorption was modeled on a 7-layer LaO-terminated symmetric non-stoichiometric $La_4Mn_3O_{10}$ (001) slab. Such 7-layer slabs have been found to suffice for a good convergence of the main properties such as $V_O^{\cdot\cdot}$ formation energy with a slab thickness[5,26,27] and are used here for consistency with a previous study. The electron charge redistribution in the terminating planes of this slab is similar to that for stoichiometric slabs with an even number of layers.[27] The total dipole moment normal to the (001) surface is naturally cancelled by the slab's symmetry, but two local dipole moments remain at the surfaces (charged surface and subsurface layer; also the adsorbate layer, if present, is charged) which are oriented in opposite directions. Transition states were calculated by the NEB method[43] with eight intermediate images. The effective atomic charges were calculated with the Bader method.[44] The atomic structures are visualized using VESTA software.[45]

3 Results and discussion

In order to finally elucidate the effect of AO *versus* MnO_2 surface terminated slabs (including the surface dipoles) on the oxygen incorporation rate, we first analyze separately the oxygen vacancy formation (Section 3.1), oxygen (O/O_2) adsorption (Section 3.2) and dissociation (Section 3.3), and then combine all these results in the discussion of the ORR kinetics in Section 3.4. In all sections, it is important to properly account for the fact that in thin symmetrical slabs, the two different terminations have different overall cation stoichiometries, and thus the average Mn oxidation states, which, in turn, affect all processes involved in the electron transfer. This issue thus far has barely been discussed in the literature. As shown in the following sections, both the surface oxygen vacancy formation and the oxygen adsorption are affected by a set of key parameters: most importantly the Mn oxidation state, reduced oxygen coordination number, lattice distortions and surface dipole effects, which are not always easy to disentangle, even through computer modelling.

3.1 Oxygen vacancy formation

In general, surface defect formation energies are expected to differ from bulk values; however, one has to carefully distinguish between the true surface effects and other contributions. In the present investigation, we use symmetrical slabs (with identical – either (La,Sr)O or MnO_2 – terminations on both sides), which have the benefits of a zero total electric dipole moment and good computational efficiency. This leads to a different overall ratio of A-site to B-site cations for AO and BO_2 terminated slabs. For the 7-layer $La_4Mn_3O_{10}$ and $La_3Mn_4O_{11}$ slabs used here, this results in Mn oxidation states of +2.67 and +3.25 (Table 1), which differ considerably from the bulk Mn^{3+} value and may strongly modify $V_O^{\cdot\cdot}$ formation and oxygen adsorption energies. This deviation should decrease asymptotically to zero for very thick slabs, but in practical calculations still directly affects the vacancy formation energy $E_{V_O^{\cdot\cdot}}$ and adsorption energies as discussed below.

For all LM and LSM compositions discussed here, the AO and BO_2 layers of the perovskite structure are charged (Table A2 in the ESI†). The layer charges for the bulk materials decrease from 0.96 *e* per formula unit for LM, down to 0.69 *e* per formula unit for LS50M (gray circles in Fig. 2), as expected for a partial substitution in the AO layers with Sr'_{La} and increasing Mn oxidation state in the BO_2 layers. While for the same average Mn oxidation state, the BO_2 layer charges for the bulk, central and

Table 1 Overview data on bulk LSM 2 × 2 × 2 supercells and symmetrical 7-layer (001) slabs[36]

	Bulk Mn	Bulk ionic charges/e				(La,Sr)O terminated slab		MnO_2 terminated slab	
x_{Sr}	Ox. state	La	Sr	Mn	O	Ox. state	Composition	Ox. state	Composition
0	+3.00	2.08		1.71	−1.27	+2.67	$La_4Mn_3O_{10}$	+3.25	$La_3Mn_4O_{11}$
0.25	+3.25	2.09	1.59	1.78	−1.25	+3.00	$La_3SrMn_3O_{10}$	+3.44	$La_{2.25}Sr_{0.75}Mn_4O_{11}$
0.50	+3.50	2.10	1.58	1.83	−1.22	+3.33	$La_2Sr_2Mn_3O_{10}$	+3.63	$La_{1.5}Sr_{1.5}Mn_4O_{11}$

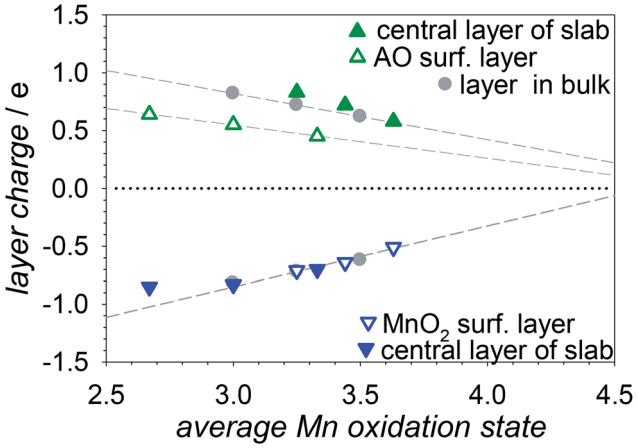

Fig. 2 Layer charges of LSM (001) (La,Sr)O and (001) MnO_2 terminated slabs. For a comparison the charges of the central slab layers and bulk LSM are also shown.

surface layers of the slabs are quite similar, and the AO surface layer charges are systematically, by 0.2–0.25 *e* per formula unit, lower than those for AO layer deeper inside the slab. Also, the splitting into sub-planes is different for AO and BO_2 surface layers (Fig. A1 in the ESI†). The surface rumpling can partially compensate for the surface dipole; for the BO_2 termination, the subsurface AO layer also shows a pronounced distortion with La/Sr outward displacement.

The decrease of the Mn oxidation state due to the variation of the La/Sr ratio and/or the formation of $V_O^{\cdot\cdot}$ affects the electronic structure of both the bulk and the slabs, so that the Fermi energy increases (it is plotted in Fig. 3a relative to the deep reference O 2s states, see ref. 36 for more details). Interestingly, different slopes are observed for the bulk and AO and BO_2 terminations. A similar effect was found for the surface work functions of the symmetrical 9-layer ABO_3 slabs, which increase more steeply for the BO_2 termination when moving through the element row, from B = Ti to Ni.[46]

Fig. 3b shows the $V_O^{\cdot\cdot}$ formation energy $E_{V_O^{\cdot\cdot}}$ for the bulk and the central layer of the slabs (*cf.* also Table A3 in the ESI†). The data for the bulk and MnO_2-terminated slabs agree very well. $E_{V_O^{\cdot\cdot}}$ in the central layer of AO terminated slabs is slightly lower, which might be affected by the electron density redistribution towards the surface AO layer with an excessive positive charge that correspondingly decreases the Mn effective oxidation state in the inner layers and lowers $E_{V_O^{\cdot\cdot}}$ (*cf.* the differences in layer charges in Fig. 2). Overall, the trend of these $E_{V_O^{\cdot\cdot}}$ with the Mn oxidation state is very similar to the variation in the bulk Fermi level (Fig. 3a). The bulk $V_O^{\cdot\cdot}$ formation energies for LM and LS50M as well as the decrease for LS50M are in good agreement with literature values in ref. 47 and 48 (with U_{eff} = 0) and experimental data on $La_{0.9}Sr_{0.1}MnO_3$, discussed in ref. 49. The fact that the bulk $E_{V_O^{\cdot\cdot}}$ is rather similar for LM and LS25M was also noticed in ref. 50, although the use of the GGA+*U* method resulted in different absolute energies.

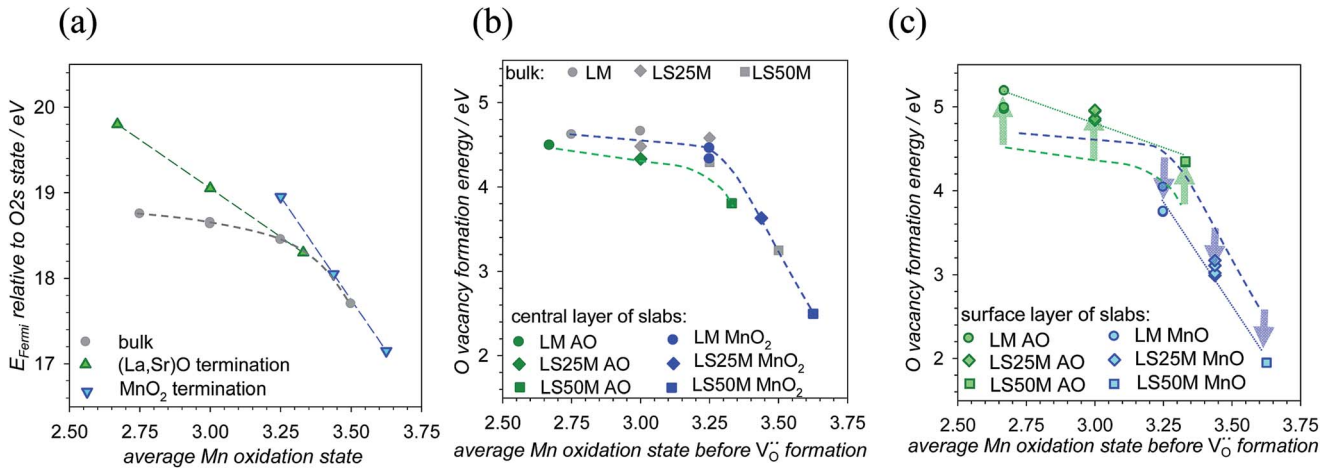

Fig. 3 (a) The Fermi level energy relative to the O 2s deep states for bulk and 7-layer slabs, and the different formal average Mn oxidation states are caused by different $V_O^{\cdot\cdot}$ concentrations (bulk) as well as La/Sr ratios (bulks and slabs). (b) Oxygen vacancy formation energy $E_{V_O^{\cdot\cdot}}$ in the bulk and in the central layer of (001) (La,Sr)O and (001) MnO_2 terminated 7-layer slabs. (c) $E_{V_O^{\cdot\cdot}}$ in the surface layers of (001) (La,Sr)O and (001) MnO_2 terminated 7-layer slabs, and the dashed lines indicate $E_{V_O^{\cdot\cdot}}$ of the respective central layers from (b).

Finally, Fig. 3c displays $E_{V_O^{\cdot\cdot}}$ for the surface oxygen vacancies (*cf.* also Table A4 in the ESI†). The difference between the symbols (surface $E_{V_O^{\cdot\cdot}}$) and dashed lines ($E_{V_O^{\cdot\cdot}}$ for bulk/central layers) can be assigned to the true surface termination effect. Note that despite some difference in the LSM absolute bulk $E_{V_O^{\cdot\cdot}}$ values between the present GGA study and the hybrid HSE approach,[51] the changes of $E_{V_O^{\cdot\cdot}}$ with the Mn oxidation state are quite comparable (for the FM state). For the BO_2 termination, $E_{V_O^{\cdot\cdot}}$ decreases with increasing Mn oxidation state with the same slope as for the bulk vacancy formation energy. The absolute formation energies are lower by ~0.5 eV (light blue arrows), which represents the true surface effect. For the AO termination, $E_{V_O^{\cdot\cdot}}$ increases with decreasing Mn oxidation state, but with a larger slope than the bulk $E_{V_O^{\cdot\cdot}}$. Consequently, the resulting true surface effect (green arrows) is most pronounced for the LM slab, for which $E_{V_O^{\cdot\cdot}}$ is by ~0.7 eV larger than the respective value for the central layer.

Fig. 4 shows the layer-resolved $E_{V_O^{\cdot\cdot}}$ values for LM, LS25M and LS50M slabs. For the central slab layer the surface formation energies closely approach the bulk values, indicating that the slab is sufficiently thick. The arrows indicate the $E_{V_O^{\cdot\cdot}}$ difference between the surface and bulk with the respective oxidation state of the slab (neglect of this issue could lead to errors exceeding 1 eV), from which the difference in surface $V_O^{\cdot\cdot}$ concentration compared to the bulk value can be estimated. However, to determine the differences in $E_{V_O^{\cdot\cdot}}$ and vacancy concentration $[V_O^{\cdot\cdot}]$ for AO and BO_2 terminations having the same average Mn oxidation state one has to refer to Fig. 3c. A similar energy difference in surface vacancy formation energies for the (001) LM LaO and MnO_2 terminations was also observed for larger, 16-layer slabs calculated using the GGA+*U* functional (these slabs were cation-stoichiometric, but exhibited a nonzero surface dipole).[28]

The true surface effect on $E_{V_O^{\cdot\cdot}}$ has two contributions: (i) contributions originating from under-coordinated atoms in the surface layer. Qualitatively, one might expect that $V_O^{\cdot\cdot}$ formation is facilitated in both termination layers, because the number of Mn–O surface chemical bonds broken upon oxygen removal is smaller compared to the bulk. This effect is well known in covalent semiconductors and the so-called *E′* centers (dangling bonds) in amorphous silica[52] as well as for perovskites with neutral surface AO and BO_2 layers such as $SrTiO_3$ (*e.g.* it was found that $E_{V_O^{\cdot\cdot}}$ is reduced by 0.8 eV on the TiO_2 termination but is almost unchanged on SrO,[28] whereas Alexandrov *et al.*[53] estimated even larger changes of 1.4 eV and 1 eV; for $BaZrO_3$, and $E_{V_O^{\cdot\cdot}}$ was reduced by 0.5 eV on the ZrO_2 termination[54]). (ii) Contributions which are related to the fact that the AO and BO_2 (001) terminations are polar. To some degree, this polarity is attenuated by small relaxations of the surface layer (outward displacement of Mn ions at the MnO_2 termination,[32] and oxide ions at the LaO termination, *cf.* Fig. A1 in the ESI†). Furthermore, in a perovskite, such as $(La,Sr)MnO_3$ with cations easily changing their oxidation state, one could expect the polarity to be partially compensated by the increased Mn oxidation state in the MnO_2 termination layer. However, the data in Table A2† indicate a less positive surface Mn charge, *i.e.* an opposite trend, which can rather be interpreted as an increased Mn–O bond covalency (but the MnO_2 surface layer charge hardly deviates from that of bulk with the same Mn oxidation state, *cf.* Fig. 2). A charge transfer of ≈+0.1 e per formula unit for the MnO_2 termination and ≈−0.15 e for the LaO surface was found in ref. 28. However, this electron density redistribution does not suffice to fully compensate for the surface dipoles, and the remaining polarity affects the defect formation and oxygen adsorption energies.

In the LaO termination layer with a formal charge of +1 *e*, the surface polarity is expected to disfavor the surface $V_O^{\cdot\cdot}$ formation. Obviously, the polarity effect dominates here over the reduced number of broken chemical bonds, leading to an overall increased $E_{V_O^{\cdot\cdot}}$. In contrast, for the MnO_2 termination, the negative excess surface charge is expected to favor $V_O^{\cdot\cdot}$ formation. Despite the additional contribution from the reduced number of broken

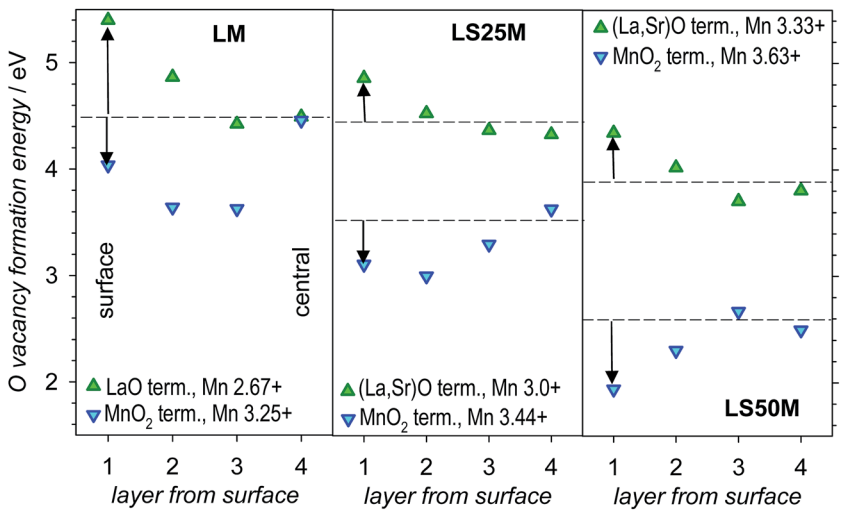

Fig. 4 The vacancy formation energies in the different layers of the (001) terminated slabs of LM (left), LS25M (middle), and LS50M (right). The arrows indicate the energy difference relative to bulk with the same average Mn oxidation state (dashed line; the same for both terminations of LM, but different for the LS25M and LS50M terminations because of the steep slope in the right hand part of Fig. 3b).

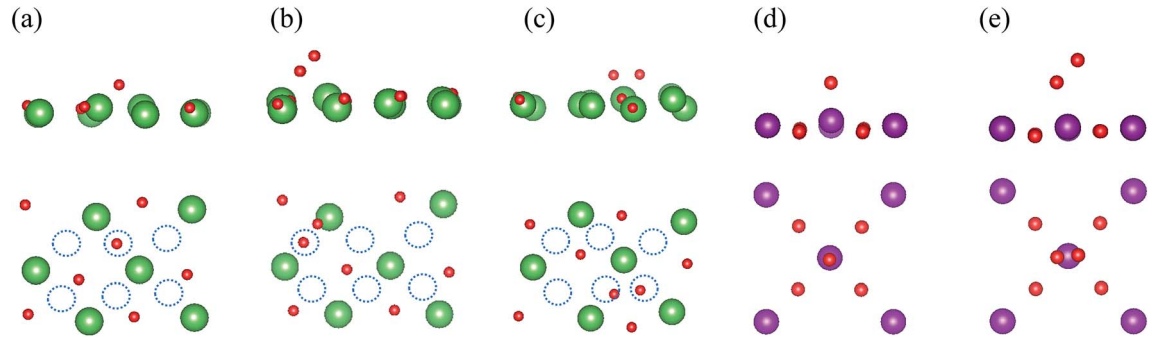

Fig. 5 Representative top (above) and side (below) views of adsorbed oxygen species on the (001) LaO termination of LM (a) atomic, (b, c) molecular tilted and horizontal, respectively. The "hollow" adsorption sites are indicated by dashed circles. (d, e) Atomic and tilted molecular oxygen species atop Mn on the (001) MnO_2 termination of LM. Red, green, and purple colors indicate O, La, and Mn ions.

bonds at the surface, the overall decrease of $E_{V_O^{\cdot\cdot}}$ at the MnO_2 termination remains quite moderate. The total difference of 1–1.2 eV in the surface $E_{V_O^{\cdot\cdot}}$ for the two terminations (for a given average Mn oxidation state) leads to a large difference in the surface $V_O^{\cdot\cdot}$ concentrations at 1000 K by more than 5 orders of magnitude (*cf.* Table A7†). This strongly affects the ORR rates, as discussed in Section 3.4. The decreased $[V_O^{\cdot\cdot}]$ on the AO termination will also make it more susceptible to effects from segregation processes or poisoning by impurities.

3.2 Atomic and molecular oxygen adsorption

Let us first discuss the adsorption of atomic O species. Our previous GGA studies[5,26] showed that atomic oxygen on the MnO_2 termination prefers to be adsorbed atop the surface Mn ion (Fig. 5d) with a binding energy of −1.1 eV (with respect to O in a gas-phase O_2 molecule). This is in qualitative agreement with the −1.9 eV found with the B3LYP hybrid functional.[55] In contrast, on the (001) LaO-terminated LM surface the only stable oxygen adsorption site is the "hollow" position (the bridge between the two nearest La ions) (Fig. 5a), in agreement with hybrid LCAO calculations,[55] plane wave GGA calculations[19] and atomic O adsorption on the LaO termination of La_2NiO_4.[56] The adsorption energy depends strongly on the Mn oxidation state (see Fig. 7a below) and can reach −4.3 eV. It might, at first glance, seem unexpected that the O is adsorbed on such a hollow site and not atop a La cation. However, this O position relative to the underlying La cations is exactly the site that O would take if a full MnO_2 layer was grown on top of the LaO layer. The La–O_{ad} distance of 2.0–2.2 Å is significantly shorter than the La–O bulk distance of ≈2.7 Å. Due to the rhombohedral distortion of the slab structure, two non-equivalent hollow positions with different adsorption energies are available, and the presence/absence of Sr leads to more configurations. The effective atomic charges, interatomic distances and the energies of adsorbed species are collected in Table A5 in the ESI†.

The O adsorbed on the AO termination carries a significant negative charge of −1.19 to −1.28 *e* (comparable to that for oxide ions) in the bulk (−1.22 to −1.27 *e*) and only slightly smaller than for O in the AO surface layer (−1.33 to −1.34 *e*), which allow us to consider it as O_{ad}^{2-} rather than O_{ad}^{-}. On the other hand, O adsorbates on another MnO_2 termination (−0.49 to −0.69 *e* on the present rhombohedral slabs and −0.62 *e* on orthorhombic slabs[5]) are less charged and should rather be considered as O_{ad}^{-}. This difference could be related to the lower electronegativity of La cations compared to Mn. The slight outward displacement of the La cations neighboring O_{ad} (Fig. 5a and 8c) further stabilizes the more negative O_{ad} charge. For LS25M slabs, the atomic O adsorption energies $E_{ads,O}$ (as well as E_{ads,O_2}) are on average by ≈0.3 eV less negative, when one Sr ion is located close to the "hollow" adsorption site (on LSM50 there is always such a Sr neighbor).

Fig. 6 summarizes the O–O bond length and charges of molecular oxygen adsorbates. This overview indicates that the assignment to superoxide or peroxide should always be based on several descriptors; in the present case the O–O bond length is a stronger criterion than the charge of the adsorbate (comparing only the charge of the superoxide species of 1.03–

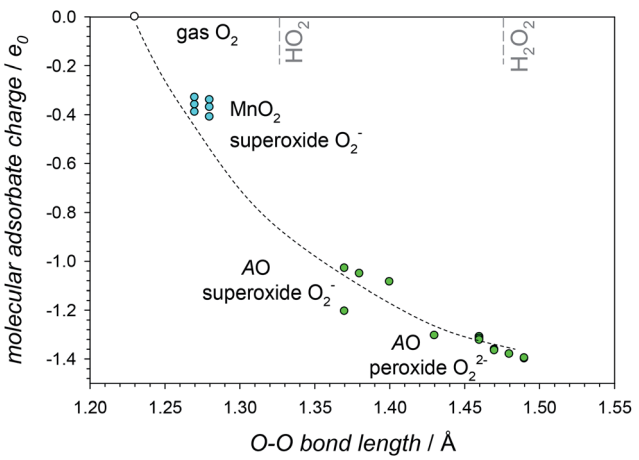

Fig. 6 Charge of molecular oxygen adsorbates on the (La,Sr)O termination and MnO_2 termination *versus* O–O bond length; for comparison gaseous O_2 is also included (bond length from DFT), and the experimental O–O bond lengths in HO_2 and H_2O_2 are indicated.[57] This plot allows for a distinction of superoxide *vs.* peroxide species. On the AO termination the superoxide not only has a shorter O–O bond than the peroxide, but also significantly larger average distances to the surface A cations (Table A5†).

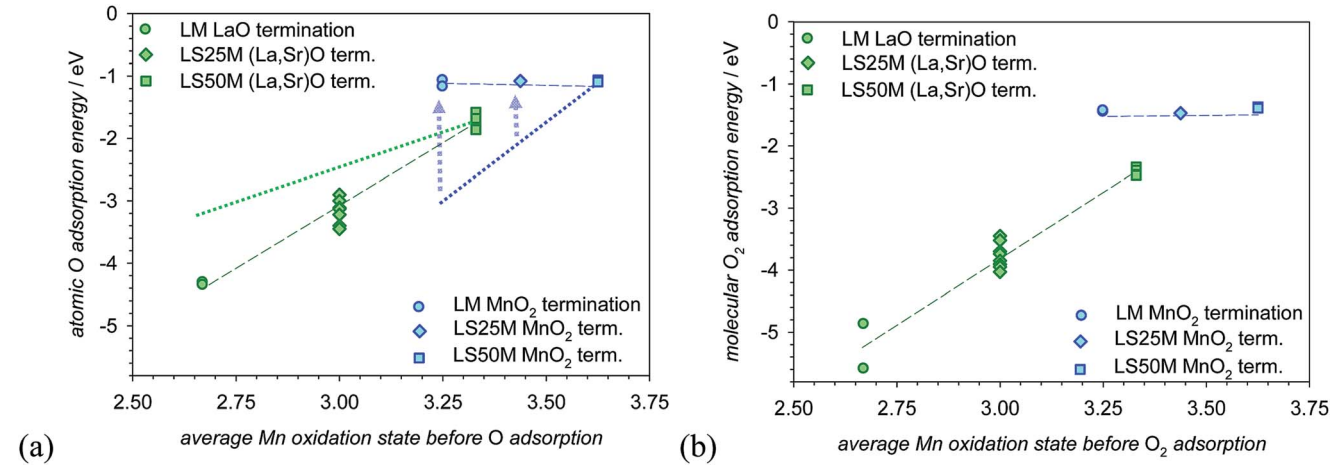

Fig. 7 (a) Atomic oxygen and (b) molecular oxygen adsorption energy as a function of the average Mn oxidation state. Dispersion in energies for the same composition and oxidation state corresponds to different adsorbate configurations as indicated in Table A5.† The dotted lines indicate the slope of the Fermi level (Fig. 3a), but with an opposite sign since electrons are transferred to adsorbed species.

1.20 e with that of bulk oxide ions, one might be tempted to assign it also to doubly charged peroxide O_2^{2-}). The comparison between MnO_2 and AO terminations also emphasizes the influence of the nature of adsorbate–slab interaction (partly covalent on MnO_2 but largely ionic on AO) on the character of the adsorbed species.

Fig. 7a shows $E_{ad,O}$ for the two different 7-layer terminations. The dotted lines indicate the expected effect of the different Mn oxidation states of the considered slabs on $E_{ads,O}$, as estimated from the variation in the slab Fermi energy in Fig. 3a. $E_{ads,O}$ on the AO termination becomes more negative with decreasing Mn oxidation state, with a much steeper slope than the slab Fermi energy. This could be caused by two contributions: (i) transfer of more than one electron per adsorbed O atom and (ii) the electrostatic attraction of negatively charged O_{ad} species with the positive charge of the AO surface layer, which is stronger for LM than LS25M and LS50M terminations. Since the O_{ad} species on AO termination roughly correspond to O_{ad}^{2-}, this stronger electron transfer can largely explain the variation of $E_{ads,O}$ (indeed, doubling the slope of the green dotted line in Fig. 7a to account for the transfer of two electrons per O reproduces very well the trend in $E_{ads,O}$). This explanation leaves only a minor role for the electrostatic contributions to $E_{ads,O}$ at the AO termination (*cf.* the smaller formal layer charges of the AO termination compared to MnO_2 in Table A2†). Most probably, the very negative adsorption energies also contain a contribution from the stabilizing effect of the adsorbed oxygen species on the AO surface plane, which otherwise attempts to mitigate the structural disruption by pronounced surface rumpling as indicated in Fig. A1.†

Despite the expected effect of the slab Fermi energy variation (blue dotted line in Fig. 7a), $E_{ad,O}$ on the MnO_2 termination is nearly independent of the Mn oxidation state. This results from the repulsion between negatively charged adsorbates O_{ad}^{-} (more negative for a lower Sr content, *cf.* Table A5†) and the negative surface layer charge (also more negative for a lower Sr content), which apparently cancels the more favorable electron transfer for Sr-poor slabs with a higher Fermi level. Thus, for the MnO_2 termination we are left with a true termination effect on O adsorption caused by the surface dipole as indicated by the blue dashed arrows; however, since the position of the blue dashed line cannot be fixed on an absolute energy scale, the picture here is only qualitative.

Fig. 7a convincingly demonstrates the importance of considering the actual Mn oxidation states caused by the slab cation stoichiometry. Indeed, a direct comparison of the atomic O adsorption energies on the LaO and MnO_2 terminations of symmetrical 7-layer slabs[55,58] or 9-layer slabs[19] yields a difference in $E_{ads,O}$ of 3–4 eV. However, Fig. 7 clearly indicates that most of this difference is due to the Mn oxidation state variation, and only less than 1 eV is the true termination effect when comparing the data for a fixed Mn oxidation state (*e.g.* $Mn^{3.3+}$).

For both terminations, the E_{ad,O_2} values for molecular adsorption are less negative than the sum of the two respective atomic O adsorption energies – *i.e.* O_2 dissociation is energetically favored. The energies, charges and distances are given in Table A5, ESI†. Molecular adsorption on the AO termination occurs in a tilted configuration (Fig. 5b), but for LS25M and LS50M also in a horizontal configuration (Fig. 5c) which yields the most negative E_{ad,O_2}. Based on the O–O bond lengths and charges (*cf.* Fig. A2 in the ESI†), the adsorption on the AO termination occurs as peroxide species (O_2^{2-}) on LM and LS25M, while on LS50M with a higher average Mn oxidation state superoxide (O_2^{-}) is also formed (however, O_2^{2-} yields the most negative E_{ads,O_2}). Peroxide species in the horizontal configuration were also found to be the most stable ones on the LaO termination of La_2NiO_4 in ref. 56, with a tilted superoxide being by 0.14 eV less favorable. On the MnO_2 termination only tilted superoxide is present (Fig. 5e). Fig. 7b shows the molecular adsorption energies; the trends and their interpretation are very similar to that of atomic adsorption.

The more negative $E_{ad,O}$ and E_{ad,O_2} for the AO termination should lead to much larger adsorbate coverages compared to the MnO_2 termination (for the same Mn oxidation state).

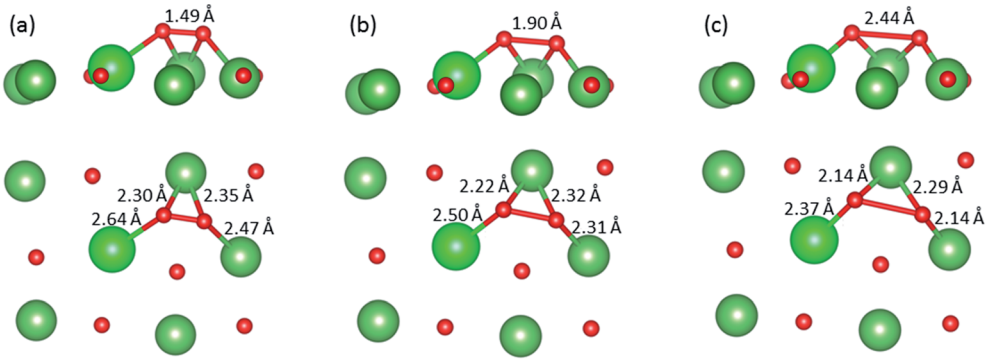

Fig. 8 Representative top and side views of oxygen dissociation on the (001) AO termination of LS25M (larger light green spheres = Sr). (a) The initial state (horizontal configuration), (b) transition state (energy higher by 0.60 eV than the initial state), and (c) one frame after the transition state (energy 0.14 eV lower than the initial state). The final state geometry is similar to that given in Fig. 9c.

However, the increase will be limited by saturation effects which arise for charged adsorbates and tend to limit the coverages to about 20%.[5] This point will become important in the kinetics discussion in the last section.

3.3 Dissociation barriers

Earlier, we have modelled in detail the dissociation of molecular oxygen species on the MnO_2 termination for an orthorhombic LM slab[5] and do not expect large differences for adsorption energies in the present slightly rhombohedrally distorted slabs. The oxygen molecule dissociation without $V_O^{\cdot\cdot}$ assistance on the defect-free AO termination is modelled here for several initial configurations. Fig. 8a illustrates the path starting from the "horizontal" LS25M configuration. The O_2 dissociation is rather a straightforward process, with simultaneous elongation of the O–O bond and gradually closer approach to the surface La/Sr ions (Fig. 8b). After dissociation, the two adsorbed O ions occupy neighboring hollow positions (Fig. 8c), with a mutual repulsion energy of $\approx$0.5 eV. The NEB-obtained O_2 dissociation barrier for this configuration is only 0.6 eV. In turn, Fig. 9 exemplifies the O_2 dissociation starting from a tilted configuration. Here the path is more complicated, since one O ion has to travel a rather large lateral distance to reach its final site, and the energy barrier also turns out to be larger, 0.9 eV.

The trends in dissociation barriers for LM, LS25M and LS50M AO-terminated slabs are revealed in Fig. 10. The energies of the dissociation transition states E_{TS} (relative to O_2 in the gas phase) become systematically more negative with the decrease of the dissociation energy ΔE_{diss} (Fig. 10a, Table A6†). Note that the ΔE_{diss} depends mainly on the average Mn oxidation state, with some additional contributions stemming from different adsorption configurations. The scattered actual dissociation barriers (Fig. 10b) show a clear trend of decrease for more negative ΔE_{diss}, which corresponds to the Bell–Evans–Polanyi principle.[59,60] Interestingly, the dissociation barrier calculated for adsorbed peroxide on the LaO termination of La_2NiO_4 (ref. 56) (1.35 eV for ΔE_{diss} = 0.4 eV) also nicely fits into this plot.

Let us now compare the O_2 dissociation barrier on the AO termination of LS50M ($Mn^{3.33+}$) with that on the LM MnO_2 termination ($Mn^{3.25+}$) since both refer to similar Mn oxidation states. On the AO termination, the barriers of 0.7–1.3 eV considerably exceed that of 0.6 eV found for the LM MnO_2 termination in ref. 5. This may be related to the dissociation pathway on AO being more complicated than on MnO_2 where it proceeds from a peroxide bridging between two surface Mn ions to two separate O atoms attached to exactly these two Mn ions. The variation of the energy barrier with Mn oxidation states is expected to be roughly similar for both terminations because a lower oxidation state (higher Fermi level) favors the electron transfer to antibonding π^* orbitals of the oxygen molecule and thus facilities the dissociation. Owing to the low $V_O^{\cdot\cdot}$ concentration in the AO surface layer, dissociation processes with $V_O^{\cdot\cdot}$ assistance are not considered for the AO termination here. For the AO termination of La_2NiO_4, a strongly decreased dissociation barrier of 0.28 eV was obtained for molecular oxygen

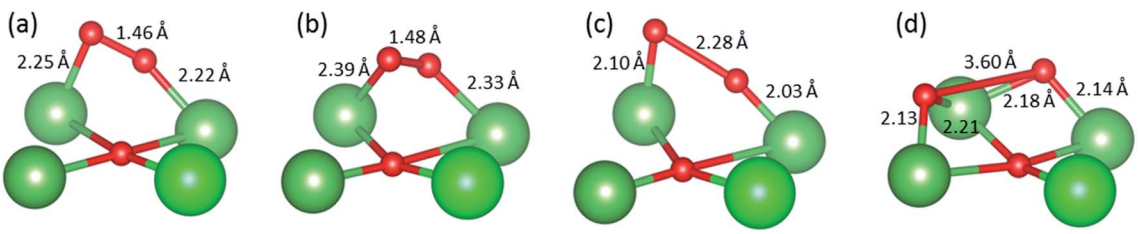

Fig. 9 Representative views of oxygen dissociation on the AO (001) termination of LS25M (larger light green spheres = Sr). (a) Initial state (tilted configuration), (b) transition state (energy 0.38 eV higher that the initial state), (c) one image after the transition state (0.33 eV higher that the initial state), and (d) final state (1.98 eV lower energy than the initial state).

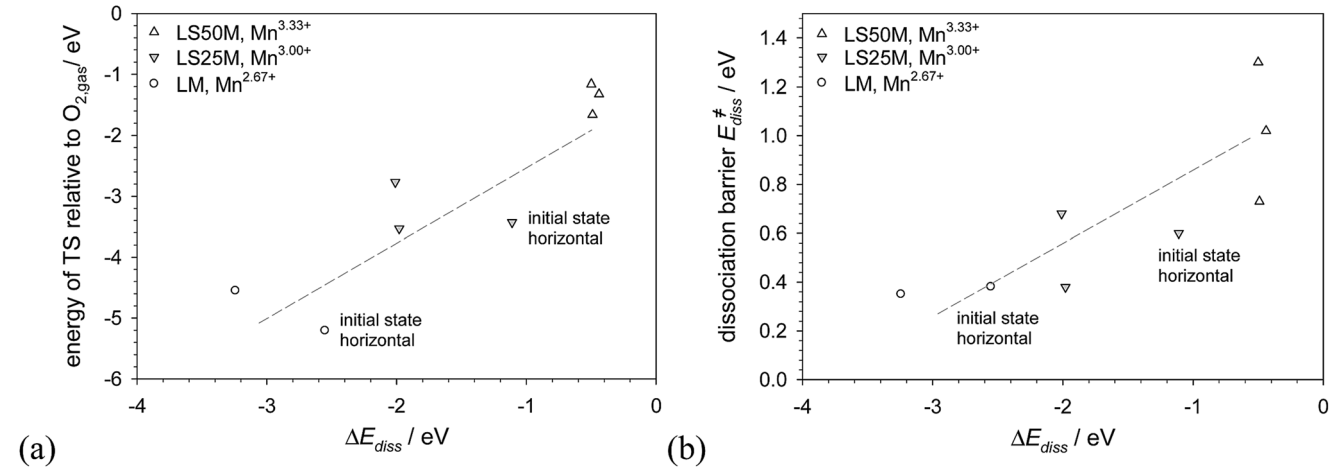

Fig. 10 (a) Energies of the dissociation transition state E_{TS} (relative to O_2 in the gas phase) on the AO termination as a function of the dissociation energy ΔE_{diss}. (b) The dissociation barrier $E^{\neq}_{diss}$ (relative to adsorbed molecular oxygen species) as a function of ΔE_{diss} (E_{TS}, $E^{\neq}_{diss}$ and ΔE_{diss} are also illustrated in Fig. 11).

species vertically inserted into a $V_O^{\cdot\cdot}$,[56] but such a reduced barrier cannot outweigh the effect of the extremely low vacancy concentration on the AO termination of the LSM slabs.

3.4 Discussion of the energy profile and kinetics for the oxygen incorporation reaction

The energy profiles for the oxygen incorporation reaction on the AO termination based on the results from the previous section are shown in Fig. 11. The overall ORR proceeds steeply downhill, being more exothermic for slabs with a low Sr content (*cf.* the larger vacancy formation energy $E_{V_O^{\cdot\cdot}}$ in Fig. 3b). However, one has to keep in mind that at realistic operational temperatures, the Gibbs free energy profile contains a large positive entropy contribution ($-T\Delta S^0 \approx 2$ eV at 1000 K) due to the loss of translational and rotational degrees of freedom of the O_2 molecule.[3] Also, the very low $V_O^{\cdot\cdot}$ concentrations in the AO surface layer significantly shift the Gibbs free energy of configurations including a vacancy to more positive values. For $La_{1-x}Sr_xMnO_{3\pm\delta}$ with $x = 0.2$, 0.5 one can estimate a bulk $V_O^{\cdot\cdot}$ concentration in the 10^{-9} range at 1000 K[5] from the

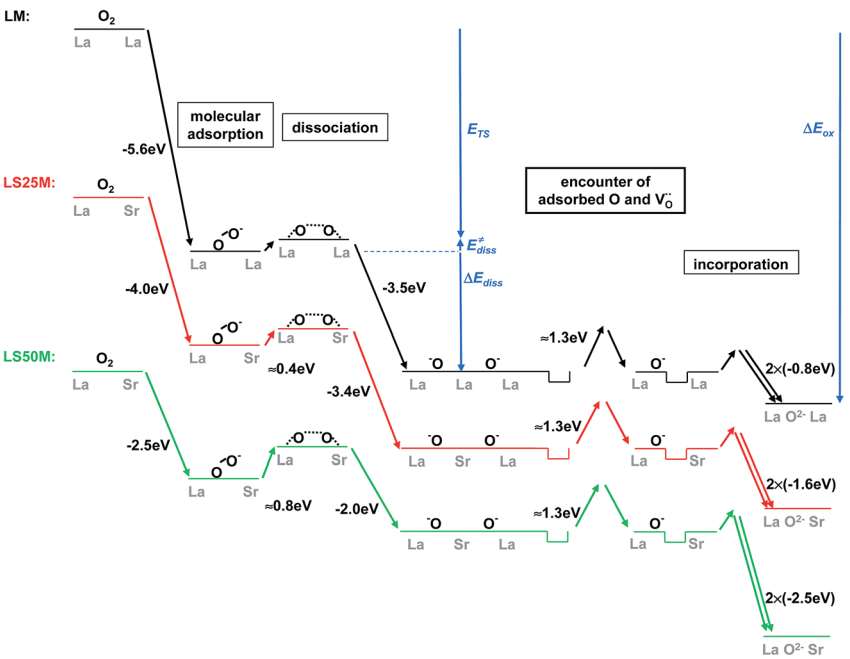

Fig. 11 Calculated energy profiles for oxygen incorporation on the LM, LS25M and LS50M (001) (La,Sr)O terminations (at zero K, no entropy effects included). The average Mn oxidation state increases from 2.67+ for LM to 3.33+ for LS50M, accompanied by the total reaction energy ΔE_{ox} becoming less exothermic from −8.8 eV to −7.4 eV for the incorporation of O_2 into two surface-layer oxygen vacancies. E_{TS} is the energy of the dissociation transition state relative to gas phase O_2, $E^{\neq}_{diss}$ is the dissociation barrier and ΔE_{diss} is the reaction energy for the dissociation.

combination of D^* and $V_O^{\cdot\cdot}$ data in ref. 61; for LM with pronounced oxygen excess[62] even lower values are expected. Such a concentration corresponds to a contribution of +1.7 eV configurational entropy at 1000 K ($-T\Delta S_{config} = RT \ln[V_O^{\cdot\cdot}]$). Thus, despite the largely downhill energy profile, the real reaction kinetics is not necessarily fast.

The $V_O^{\cdot\cdot}$ formation energies for the AO termination are higher by 0.5–0.7 eV compared to bulk with a comparable Mn oxidation state (Fig. 3c). At 1000 K this corresponds to a decrease of the $V_O^{\cdot\cdot}$ concentration by roughly 3 to 4 orders relative to the bulk (these numbers are compiled in Table A7†). Therefore, ORR mechanisms which proceed *via* direct O_2 adsorption into a $V_O^{\cdot\cdot}$ on the AO termination can be ruled out. In other words, the thermally activated dissociation rate of $O_{2,ad}{}^{2-}$ adsorbed on the perfect AO termination is higher than the rate of O_2 adsorption into a surface $V_O^{\cdot\cdot}$ followed by subsequent fast dissociation.

Both the atomic and molecular oxygen adsorption energies on AO terminations are very negative (range of −4.5 to −2 eV per O Fig. 7a and −5 to −2.5 eV per O_2 Fig. 7b). This means that at SOFC operating temperatures in air the concentration of adsorbed oxygen species could become so high that it reaches the plateau of ∼20% coverage, limited by the mutual repulsion of charged adsorbates.[5,63] The adsorbate coverages calculated with reasonably estimated ΔS^0_{add} values are also given in Table A7.† Because of the more negative ΔH^0_{add} for the formation of two atomic species compared to one molecular adsorbate (Fig. 7a and b), $O_{ad}{}^{2-}$ on AO and $O_{ad}{}^{-}$ on MnO_2 are always in majority. Only for molecular oxygen species on the MnO_2 termination, smaller coverages in the range of 10^{-4} to a few % are obtained. This means that the molecular adsorbate coverage on the AO termination is increased from these values to the saturation limit of ≈20%, *i.e.* varying by a factor of 4 to 2000. Since the chemisorption is assumed to proceed without a significant barrier, this is not the rate limiting step.

Three processes could be potentially considered as the rate determining step on the AO termination: (i) the O_2 dissociation, with a barrier of 0.1–0.8 eV (Fig. 11), (ii) the encounter of $O_{ad}{}^{2-}$ species with a $V_O^{\cdot\cdot}$, and (iii) the final incorporation of an atomic $O_{ad}{}^{2-}$ species into a neighboring $V_O^{\cdot\cdot}$. For the MnO_2 termination, step (iii) was found to occur with no barrier,[5] and also on the AO termination it is reasonable to assume that it proceeds fast. For step (ii), $V_O^{\cdot\cdot}$ migration exclusively in the LaO surface layer is not possible since in perovskites the O migration path/transition state configuration always contains in the transition state a B-site cation.[37,64] Thus, $V_O^{\cdot\cdot}$ jumps from/to the subsurface MnO_2 layer must be involved, with a barrier that comprises the (bulk) $V_O^{\cdot\cdot}$ migration barrier of 0.95 eV[5,26] and additional contribution from the unfavorable configuration of $V_O^{\cdot\cdot}$ being in the surface layer (about 0.5 eV, Fig. 4), resulting in an effective migration energy of 1.4 eV. On the other hand, the $O_{ad}{}^{2-}$ migration barrier on the AO surface layer amounts to 1.3 eV. So the migration of $V_O^{\cdot\cdot}$ to $O_{ad}{}^{2-}$ and *vice versa* contribute equally to the $V_O^{\cdot\cdot} - O_{ad}{}^{2-}$ encounter. An encounter of peroxide ions with surface $V_O^{\cdot\cdot}$ followed by a dissociation (case (iii)) would yield a lower rate than the $V_O^{\cdot\cdot} - O_{ad}{}^{2-}$ encounter because of the lower peroxide coverage compared to O_{ad}. This mutual approach is also expected to be slower than the dissociation step (i) because it involves $V_O^{\cdot\cdot}$ which exhibits extremely low concentrations (see above and Table A7†) while the coverage of adsorbed superoxide or peroxide ions as the precursor for the dissociation is high. Summing up, we conclude that the mutual approach of $V_O^{\cdot\cdot}$ and $O_{ad}{}^{2-}$ could be regarded as the rate determining step on the AO termination.

Notwithstanding the fact that the same step is rate determining for the AO and MnO_2 terminations (at least, at comparably high pO_2 (ref. 5) as relevant for a cathode material), the ORR is expected to be much slower for the former termination. On one hand, the adsorption energies for atomic as well as molecular oxygen species are much more negative on the AO termination compared to MnO_2 (for the same Mn oxidation state), but since the coverage by charged adsorbates approaches a saturation at about 20%[5] this more favorable adsorption energetics can only partially be translated into a higher concentration of $O_{2,ad}{}^{-/2-}$ and $O_{ad}{}^{-/2-}$ (the latter being the relevant concentration for the rate determining step). On the other hand, the surface $V_O^{\cdot\cdot}$ concentration is lower by more than 5 orders of magnitude on the AO termination, and the migration barrier for the $O_{ad}{}^{2-} - V_O^{\cdot\cdot}$ encounter is more than 0.6 eV higher (Table A7†) which corresponds to a 3 orders of magnitude decrease of the $O_{ad}{}^{2-} - V_O^{\cdot\cdot}$ encounter rate at 1000 K. Although these numbers are only a rough estimate, it indicates that even if most of the surface on a real SOFC cathode has a (La,Sr)O termination, even small patches of the MnO_2 termination (or any other terminations more active than (La,Sr)O) in the percent range might still make a significant contribution to the overall ORR kinetics. This is in line with the observation for thin film $La_{0.6}Sr_{0.4}CoO_{3-\delta}$ cathodes that already the addition of a monolayer of only 4% Sr strongly decreases the exchange rate of a freshly deposited film.[65] While we are not aware of direct experimental determinations of adsorbed oxygen coverage on exclusively AO- or BO_2-terminated perovskites, a recent ambient-pressure XPS investigation demonstrated distinct differences in the water adsorption of LaO- and FeO_2-terminated $LaFeO_3$.[66]

4 Conclusions

The energetics of $V_O^{\cdot\cdot}$ formation as well as molecular and atomic oxygen adsorption were analyzed and compared for the polar (La,Sr)O and MnO_2 (001) terminations of (La,Sr)MnO_3 slabs. Distinct differences are noticed (more negative adsorption energies and higher $V_O^{\cdot\cdot}$ formation energies for the (La,Sr)O termination), which can however not be rationalized with a simple electrostatic picture. For comparably thin symmetrical slabs (used in practical calculations), the effect of cation off-stoichiometry also has to be considered, which affects the average Mn oxidation state (neglecting this may lead to errors of several eV). When comparing data for the same Mn oxidation state, $V_O^{\cdot\cdot}$ formation energy is higher by 1–1.2 eV in the (La,Sr) surface layer than for the MnO_2 termination, which drastically decreases $[V_O^{\cdot\cdot}]$ (also relative to bulk). Interestingly, not only the adsorption energies differ between the terminations, but also the adsorbate charges ($O_{2,ad}{}^{2-}$ and $O_{ad}{}^{2-}$ for (La,Sr)O but rather $O_{2,ad}{}^{-}$ and $O_{ad}{}^{2-}$ for MnO_2). The fact that the adsorption

energies are much more negative on the (La,Sr)O termination can only partly be translated into higher adsorbate coverages, because they meet the saturation limit of about 20% for charged species. For both terminations, an encounter of adsorbed atomic oxygen species and $V_O^{\cdot\cdot}$ is expected to be the rate determining step of oxygen exchange, and the extremely low surface $V_O^{\cdot\cdot}$ concentration predicts the rate on the (La,Sr)O termination to be much slower than that on MnO_2. Thus, the MnO_2 terminated fraction of the (La,Sr)MnO_3 polar surfaces is expected to mainly contribute to the oxygen reduction reaction even if present in only small amounts.

The main trends found here for the (La,Sr)MnO_3 system (decreased $[V_O^{\cdot\cdot}]$ and increased adsorbate coverage on the AO termination) are expected to hold also for related (Ba,Sr,La)(Fe,Co,Mn)O_3 perovskite cathode materials. However, the detailed dependence on the cation composition is far from trivial to predict since the decreased $[V_O^{\cdot\cdot}]$ and increased adsorbate coverage exert a counteracting effect on the oxygen exchange rate. The contribution of the AO termination to the overall rate is expected to become larger in materials with a less negative oxidation energy which increases the bulk $[V_O^{\cdot\cdot}]$ and typically makes the adsorption energies less negative (*i.e.* decreases adsorbate coverages). Then, a larger part of the more negative adsorption energy for the AO termination may actually translate into increased oxygen coverages before the saturation limit is met.

Conflicts of interest

There are no conflicts of interest to declare.

Acknowledgements

This research was partly funded by the Latvian project IMIS2 with the computer resources provided by the High Performance Computing Centre Stuttgart (HLRS) (Project DEFTD 12939). The authors thank D. Gryaznov for fruitful discussions and M. Sokolov for technical assistance. MMK is grateful to the Office of the Director of National Science Foundation for support under the Independent Research and Development program. The findings, conclusions, and recommendations expressed in this material are those of the authors and do not necessarily reflect the views of NSF and other funding agencies.

References

1 A. J. Jacobson, *Chem. Mater.*, 2010, **22**, 660.
2 A. Aguadero, L. Fawcett, S. Taub, R. Woolley, K. T. Wu, N. Xu, J. A. Kilner and S. J. Skinner, *J. Mater. Sci.*, 2012, **47**, 3925.
3 M. M. Kuklja, E. A. Kotomin, R. Merkle, Y. A. Mastrikov and J. Maier, *Phys. Chem. Chem. Phys.*, 2013, **15**, 5443.
4 E. A. Kotomin, R. Merkle, Y. A. Mastrikov, M. M. Kuklja and J. Maier, in *Computational Approaches to Energy Materials*, ed. A. Walsh, A. A. Sokol and C. R. A. Catlow, John Wiley & Sons, 2013, Ch. 6.
5 Y. A. Mastrikov, R. Merkle, E. Heifets, E. A. Kotomin and J. Maier, *J. Phys. Chem. C*, 2010, **114**, 3017.
6 S. Piskunov, E. Heifets, T. Jacob, E. A. Kotomin, D. E. Ellis and E. Spohr, *Phys. Rev. B*, 2008, **78**, 121406.
7 R. Herger, P. R. Willmott, C. M. Schlepütz, M. Björck, S. A. Pauli, D. Martoccia, B. D. Patterson, D. Kumath, R. Clarke, Y. Yacoby and M. Döbeli, *Phys. Rev. B*, 2008, **77**, 985401.
8 T. T. Fister, D. D. Fong, J. A. Eastman, P. M. Baldo, M. J. Highland, P. H. Fuoss, K. R. Balasubramaniam, J. C. Meador and P. A. Salvador, *Appl. Phys. Lett.*, 2008, **93**, 151904.
9 K. Katsiev, B. Yildiz, K. R. Balasubramaniam and P. A. Salvador, *Appl. Phys. Lett.*, 2009, **95**, 092106.
10 W. Lee, J. W. Han, Y. Chen, Z. Cai and B. Yildiz, *J. Am. Chem. Soc.*, 2013, **135**, 7909.
11 Z. Cai, M. Kubicek, J. Fleig and B. Yildiz, *Chem. Mater.*, 2012, **24**, 1116.
12 E. Bucher, W. Sitte, F. Klauser and E. Bertel, *Solid State Ionics*, 2011, **191**, 61.
13 J. Druce, H. Tellez, M. Burriel, M. D. Sharp, L. J. Fawcett, S. N. Cook, D. S. McPhail, T. Ishihara, H. H. Brongersma and J. A. Kilner, *Energy Environ. Sci.*, 2014, **7**, 3593.
14 C. Noguera, *J. Phys.: Condens. Matter*, 2000, **12**, R367.
15 C. Noguera and J. Goniakowski, *Chem. Rev.*, 2013, **113**, 4073.
16 E. Heifets, W. A. Goddard III, E. A. Kotomin, R. I. Eglitis and G. Borstel, *Phys. Rev. B*, 2004, **69**, 035408.
17 P. P. Dholabhai, R. Perrot and B. P. Uberuaga, *J. Phys. Chem. C*, 2016, **120**, 10485.
18 M. Setvin, M. Reticcioli, F. Poelzleiter, J. Hulva, M. Schmid, L. A. Boatner, C. Franchini and U. Diebold, *Science*, 2018, **359**, 572.
19 G. Pilania and R. Ramprasad, *Surf. Sci.*, 2010, **64**, 1889.
20 G. Pilania, P. X. Gao and R. Ramprasad, *J. Phys. Chem. C*, 2012, **116**, 26349.
21 J. Mizusaki, N. Mori, H. Takai, Y. Yonemura, H. Minamiue, H. Tagawa, M. Dokiya, H. Inaba, K. Naraya, T. Sasamoto and T. Hashimoto, *Solid State Ionics*, 2000, **129**, 163.
22 W. Kohn and L. J. Sham, *Phys. Rev.*, 1965, **140**, A1133.
23 G. Kresse and J. Furthmüller, *Phys. Rev. B*, 1996, **54**, 11169.
24 G. Kresse and D. Joubert, *Phys. Rev.*, 1999, **59**, 1758.
25 J. P. Perdew, K. Burke and M. Ernzerhof, *Phys. Rev. Lett.*, 1996, **77**, 3865.
26 E. A. Kotomin, Y. A. Mastrikov, E. Heifets and J. Maier, *Phys. Chem. Chem. Phys.*, 2008, **10**, 4644.
27 E. A. Kotomin, R. A. Evarestov, Y. A. Mastrikov and J. Maier, *Phys. Chem. Chem. Phys.*, 2005, **7**, 2346.
28 Y. L. Lee and D. Morgan, *Phys. Rev. B*, 2015, **91**, 195430.
29 W. L. Huang, Q. Zhu, W. Ge and H. Li, *Comput. Mater. Sci.*, 2011, **50**, 1800.
30 A. L. Gavin and G. W. Watson, *Solid State Ionics*, 2017, **299**, 13.
31 Z. Xu, J. Rossmeisl and J. R. Kitchin, *J. Phys. Chem. C*, 2015, **119**, 4827.
32 Y. A. Mastrikov, *PhD thesis*, University of Stuttgart, Germany, 2008.
33 R. Merkle, Y. A. Mastrikov, E. A. Kotomin, M. M. Kuklja and J. Maier, *J. Electrochem. Soc.*, 2012, **159**, B219.

34 M. M. Kuklja, Y. A. Mastrikov, B. Jansang and E. A. Kotomin, *J. Phys. Chem. C*, 2012, **116**, 18605.
35 D. Fuks, Y. Mastrikov, E. A. Kotomin and J. Maier, *J. Mater. Chem. A*, 2013, **1**, 14320.
36 E. A. Kotomin, R. Merkle, Y. A. Mastrikov, M. M. Kuklja and J. Maier, *ECS Trans.*, 2017, 77(10), 67.
37 Y. A. Mastrikov, R. Merkle, E. A. Kotomin, M. M. Kuklja and J. Maier, *Phys. Chem. Chem. Phys.*, 2013, **15**, 911.
38 H. J. Monkhorst and J. D. Pack, *Phys. Rev. B*, 1976, **13**, 5188.
39 B. Hauback, H. Fjellvåg and N. Sakai, *J. Solid State Chem.*, 1996, **124**, 43.
40 R. Hammami, N. H. Batis, H. Batis and C. Minot, *Solid State Sci.*, 2009, **11**, 885.
41 E. A. Ahmad, V. Tilei, D. Kramer, G. Mallia, K. A. Stoerzinger, Y. Shao-Horn, A. R. Kucernak and N. M. Harrison, *J. Phys. Chem. C*, 2015, **118**, 16804.
42 E. Symianakis, D. Malko, E. Ahmad, A. S. Mamede, J. F. Paul, N. Harrison and A. Kucernak, *J. Phys. Chem. C*, 2015, **119**, 12209.
43 G. Henkelman and H. Jonsson, *J. Chem. Phys.*, 2000, **113**, 9978.
44 G. Henkelman, A. Arnaldsson and H. Jonsson, *Comput. Mater. Sci.*, 2006, **36**, 354.
45 K. Momma and F. Izumi, *IUCr Newslett.*, 2006, **7**, 106–119.
46 R. Jacobs, J. Booske and D. Morgan, *Adv. Funct. Mater.*, 2016, **26**, 5471.
47 Y. M. Choi, M. C. Lin and M. L. Liu, *J. Power Sources*, 2010, **195**, 1441.
48 Y. L. Lee, J. Kleis, J. Rossmeisl and D. Morgan, *Phys. Rev. B*, 2009, **80**, 224101.
49 D. S. Mebane, Y. Liu and M. Liu, *Solid State Ionics*, 2008, **178**, 1950.
50 L. Y. Gan, S. O. Akande and U. Schwingenschlögl, *J. Mater. Chem. A*, 2014, **2**, 19733.
51 M. Pavone, A. B. Munoz-Garcia, A. M. Ritzman and E. A. Carter, *J. Phys. Chem. C*, 2014, **118**, 13346.
52 A. M. El-Sayed, M. B. Watkins, V. Afanas'ev and A. L. Shluger, *Phys. Rev. B*, 2014, **89**, 125201.
53 V. E. Alexandrov, E. A. Kotomin, J. Maier and R. A. Evarestov, *Eur. J. Phys. B*, 2009, **72**, 53.
54 T. S. Bjorheim, M. Arrigoni, S. W. Saed, E. Kotomin and J. Maier, *Chem. Mater.*, 2016, **28**, 1363.
55 S. Piskunov, T. Jacob and E. Spohr, *Phys. Rev. B*, 2011, **83**, 073402.
56 T. Akbay, A. Staykov, J. Druce, H. Tellez, T. Ishihara and J. A. Kilner, *J. Mater. Chem. A*, 2016, **4**, 13113.
57 *NIST Computational Chemistry Comparison and Benchmark Database*, ed. R. D. Johnson III, American Chemical Society, Washington DC, 14th edn, 2006.
58 Y. L. Lee, M. J. Gadre, Y. Shao-Horn and D. Morgan, *Phys. Chem. Chem. Phys.*, 2015, **17**, 21643.
59 R. P. Bell, *Proc. R. Soc. London, Ser. A*, 1936, **154**, 414.
60 M. G. Evans and M. Polanyi, *J. Chem. Soc., Faraday Trans.*, 1936, **32**, 1340.
61 R. A. De Souza and J. A. Kilner, *Solid State Ionics*, 1998, **106**, 175.
62 J. Mizusaki, N. Mori, H. Takai, Y. Yonemura, H. Minamiue, H. Tagawa, M. Dokiya, H. Inaba, K. Naraya, T. Sasamoto and T. Hashimoto, *Solid State Ionics*, 2000, **129**, 163.
63 J. Fleig, R. Merkle and J. Maier, *Phys. Chem. Chem. Phys.*, 2007, **9**, 2713.
64 J. A. Kilner and R. J. Brook, *Solid State Ionics*, 1982, **6**, 237.
65 G. M. Rupp, A. K. Opitz, A. Nenning, A. Limbeck and J. Fleig, *Nat. Mater.*, 2017, **16**, 640.
66 K. A. Stoerzinger, R. Comes, S. R. Spurgeon, S. Thevuthasan, K. Ihm, E. J. Crumlin and S. A. Chambers, *J. Phys. Chem. Lett.*, 2017, **8**, 1038.